scientific reports

Check for updates

OPEN

Highly efficient self-powered perovskite photodiode with an electron-blocking hole-transport NiO_x layer

Amir Muhammad Afzal, In-Gon Bae, Yushika Aggarwal, Jaewoo Park, Hye-Ryeon Jeong, Eun Ha Choi & Byoungchoo Park✉

Hybrid organic–inorganic perovskite materials provide noteworthy compact systems that could offer ground-breaking architectures for dynamic operations and advanced engineering in high-performance energy-harvesting optoelectronic devices. Here, we demonstrate a highly effective self-powered perovskite-based photodiode with an electron-blocking hole-transport layer (NiO_x). A high value of responsivity ($R = 360$ mA W^{-1}) with good detectivity ($D = 2.1 \times 10^{11}$ Jones) and external quantum efficiency ($EQE = 76.5\%$) is achieved due to the excellent interface quality and suppression of the dark current at zero bias voltage owing to the NiO_x layer, providing outcomes one order of magnitude higher than values currently in the literature. Meanwhile, the value of R is progressively increased to 428 mA W^{-1} with $D = 3.6 \times 10^{11}$ Jones and $EQE = 77\%$ at a bias voltage of − 1.0 V. With a diode model, we also attained a high value of the built-in potential with the NiO_x layer, which is a direct signature of the improvement of the charge-selecting characteristics of the NiO_x layer. We also observed fast rise and decay times of approximately 0.9 and 1.8 ms, respectively, at zero bias voltage. Hence, these astonishing results based on the perovskite active layer together with the charge-selective NiO_x layer provide a platform on which to realise high-performance self-powered photodiode as well as energy-harvesting devices in the field of optoelectronics.

There is strong demand for high-performance photodetector devices owing to their favourable potential for both civilian and military use in light-detecting devices such as light-imaging sensors and applications such as night-time surveillance[1,2]. Specifically, light-harvesting materials and devices which convert photons to electricity have become the core components of several types of advanced optical technology[3]. For instance, silicon-based structures such as metal–oxide–semiconductors (MOS) are used in modern optoelectronic industries for the purposes of optical communications and are used in high sensitivity image processing cameras. However, serious breakdowns can occur in MOS-based photodetectors due to the high leakage current triggered by their thin oxide layers[4].

Currently, instead of MOS, perovskite materials show numerous attractive characteristics, such as ambipolar transport, bandgap tuning, high external quantum efficiency (*EQE*), considerable optical absorption, and long charge carrier diffusion lengths, all of which form the main key parameters for optoelectronic devices, especially for photovoltaic (PV) cells and photodetectors[5,6]. Many complex perovskite composites can be perceived as striking substitutes to silicon-based photodetectors and imaging sensors. For example, smooth, highly crystallised, and pinhole-free Sn- and Pb-rich binary perovskite composite films can be critical material systems in the effort to realise efficient photodetectors[7,8]. Such perovskite-based self-powered photodetectors show an extraordinary responsivity (R) value of 0.2 A W^{-1} at 940 nm and a fast response time of 2.27 µs, exceeding those of most silicon-based imaging sensors. Specifically, perovskite composites of $CH_3NH_3PbX_3$ (X = Br, Cl, and I) have also attracted much attention in relation to optoelectronic technology given their potential for enhanced performance, with one example being light-harvesting devices[9,10]. Thus, Hu et al. fabricated a lateral type of photodiode based on perovskite ($CH_3NH_3PbI_3$) and measured the responsivity R and *EQE* at a high bias voltage ($V_{bias} = 2$ V)[11]. Further, Chen et al. demonstrated perovskite photodiode which utilise graphene as an electrode and found relatively small values of R (22 mA W^{-1}) and detectivity (D) (3.55×10^9 Jones)[12]. Zhou et al. established a perovskite photodiode with R values of approximately 198 mA W^{-1}[13]. However, the prevailed fabrication methods and

Department of Electrical and Biological Physics, Kwangwoon University, Wolgye-Dong, Seoul 01897, South Korea. ✉email: bcpark@kw.ac.kr

strategies reported thus far will inevitably lead to grain boundary issues and large variations in the morphologies of the resultant perovskite active layers in the devices. Further, the relatively small values of the responsivity *R* and detectivity *D* of perovskite photodiodes and their comparatively large dark current densities are the major hurdles to overcome to realise high-performance devices. Moreover, suitable materials capable of forming a good interface with the perovskite active layer remain elusive in the field of perovskite-based photodiode during the effort to achieve high *R* and *D* values as well as fast response times. Thus, the device performance capabilities of recent perovskite-based photodiode remain insufficient.

Meanwhile, researchers remain motivated to realise an innovative photodiode exhibiting astonishing performance and a high *R* value using other functional layers as hole transport layers (HTLs) and electron transport layers (ETLs) together with hybrid heterostructures exhibiting tailored, novel, and improved characteristics[14–16]. In order to achieve excellent device performance with regard to photoconductivity, the proper selection of the HTLs is crucial, not only to decrease the dark current density but also to enhance and promote perfect light absorption of the perovskite active layer in the wide visible region[17–19]. Metal-oxide (MO) or ternary MO nanoparticles (NPs) synthesised by a solution process are favourable for unlocking their potential in solar cells as HTLs given their low cost, good stability, and promising optical characteristics. However, exotic organic ligands adopted for the purpose of ensuring a small size and a nano-dispersion are associated with poor conductivity, which thus impedes their use in electrical applications[20]. Well-dispersed $NiCo_2O_4$ ternary MO NPs synthesised by a unique method without exotic ligands have been used successfully as a HTL in PVSCs. The pinhole-free films of $NiCo_2O_4$ NPs facilitated the formation of large grains of perovskite films. As a result, the power conversion efficiency (PCE) was enhanced to 18%, with promising stability[21]. Other ternary MO NPs of In-doped $CuCrO_2$ have also been proposed as an efficient HTL material system. Interestingly, the PCE of the PVSCs with the In:$CuCrO_2$ HTL was increased to 20.5% with good repeatability and photostability[22]. Thus, new approaches are mandatory for the realisation of excellent perovskite photodiode using heterostructures of organic and inorganic materials combined with perovskite materials.

Recently, among inorganic semiconductor thin films, nickel oxide (NiO_x) has been considered as a crucial building block for modern optoelectronic devices owing to its versatile physical and chemical features along with its appropriate band structure. Specifically, NiO_x has been used in organic and perovskite PV cells as a HTL owing to its efficient chemical and thermal stability, outstanding hole-transport characteristics, large band gap (> ~ 3.7 eV), the ability to control the valence-band energy level effectively, and its deep valence band position (> 5.2 eV)[23–25]. Chen et al. used a NiO_x HTL synthesised by a sputtering method at a low temperature to devise inverted-type perovskite PV cells, achieving a PCE of 11.6%[26]. Zhu et al. introduced a solution-processed NiO_x:PbI_2 nanocomposite structure which operated at room-temperature to assist with compact and crystalline $MAPbI_3$ film growth, which is critical during the fabrication of effectual photodetectors. This nanocomposite served as an electron-blocking, hole-extracting, and passivation layer and ultimately suppressed the dark current, resulting in improved photo characteristics, such as better detectivity and faster response times[27]. More recently, a thin interlayer of NiO_x, synthesised by a comparatively simple solution-processed method demonstrated tunable work functions (5.0 – 5.6 eV) and efficient hole conductivity outcomes[28,29]. A thin layer of NiO_x as a HTL in perovskite PV cells was also shown to hinder the penetration of water and oxygen into a device effectively[30]. Zin et al. proposed a simple method by which to synthesise a NiO_x layer and used it as a HTL in inverted perovskite PV cells. Their device showed greatly improved values of PCE (~ 20.2%)[24,31]. Particularly, a thin NiO_x film showed enhanced charge carrier density and conductivity through improvements of the interfacial charge extraction, thus reducing the interface trap density and providing better energy level alignment with the perovskite layer in perovskite solar cells[32].

Inspired by these remarkable characteristics of NiO_x layers, a heterostructure approach which involves the assembly of a halide perovskite with the inorganic semiconducting material of NiO_x may represent an alternative means by which to design photodiode that are anticipated to have enhanced photosensitivity. In this work, a high-performance and unique perovskite photodiode with a HTL of NiO_x exhibiting a high responsivity value is reported. We designed a self-powered hybrid perovskite-based photodiode structure that suppresses the dark leakage current and enhances the performance of the perovskite photodiode. The effects of the HTL of NiO_x in the perovskite photodiode on the device performance and limitation factors are investigated by evaluating the optoelectronic characteristics of the photodiode. We measured the optoelectronic characteristics of the photodiode device under different power levels and wavelengths of incident laser light to obtain the *R*, *D*, and *EQE* values at a given bias voltage. Further, we took temporal photoresponse measurements to determine the response time (rise and decay time) characteristics. We also verified the *EQE* values through incident-photon-to-electron conversion efficiency (IPCE) measurements and confirmed the degree of self-consistency in the results. Moreover, we measured the characteristics of reference devices with poly (3, 4-ethylene dioxythiophene) polystyrene sulfonate (PEDOT:PSS) as a HTL in order to compare and support our results, showing that NiO_x as a HTL exhibits much improved photodiode performance as compared to the conventional HTL of PEDOT:PSS.

Results

Initially, in order to understand the surface properties of the fabricated sample NiO_x and reference PEDOT:PSS layers, atomic force microscopy (AFM), Kelvin probe force microscopy (KPFM), and contact angle measurements were utilised to characterise the layers, especially with regard to their surface roughness and surface potential levels. Figure 1a,b correspondingly show the observed results of the AFM topologies and KPFM surface potential maps of the NiO_x and PEDOT:PSS layers coated onto indium tin oxide (ITO) substrates. The nearly identical roughness values of the NiO_x and PEDOT:PSS layers were approximately 0.73 nm. Thus, the fabricated NiO_x layer on the ITO substrate is quite flat and uniform. From the obtained KPFM surface potential maps, we also

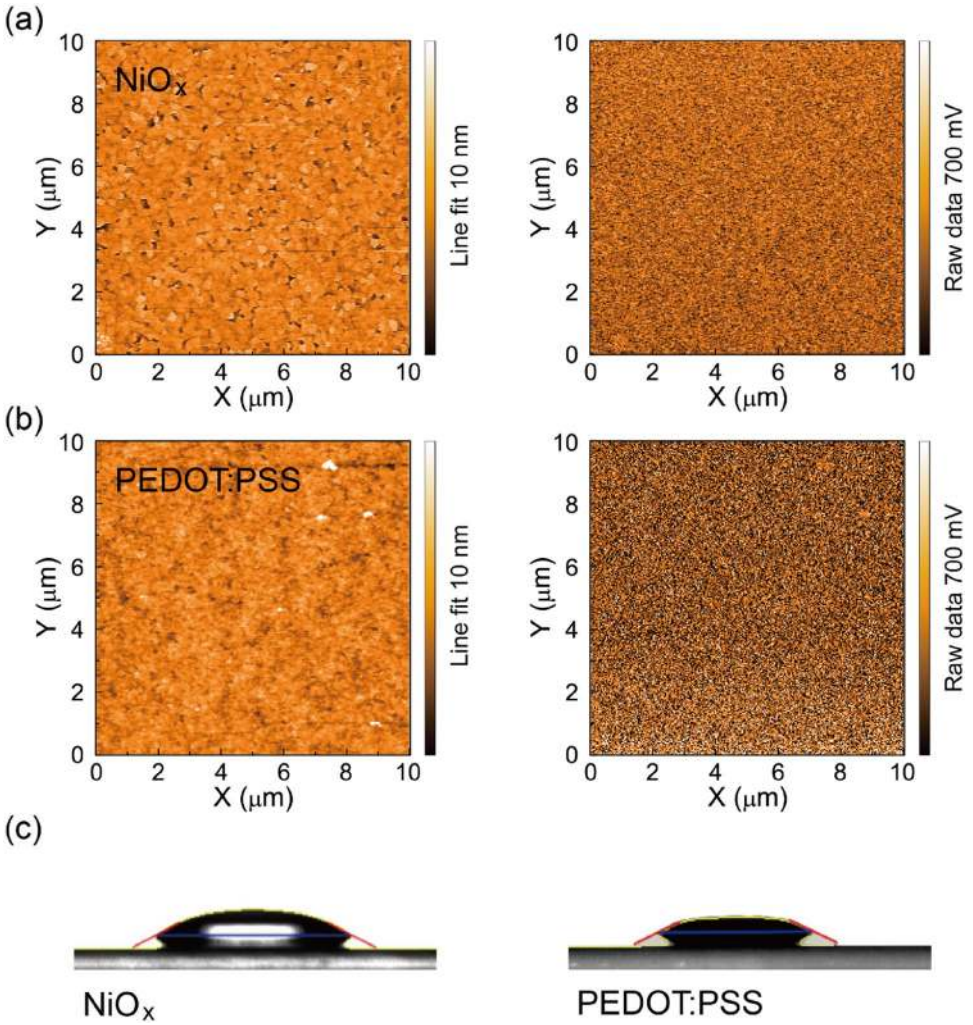

Figure 1. AFM (left) and KPFM (right) images of a sample NiO_x layer (**a**) and a reference PEDOT:PSS layer (**b**), and (**c**) water contact angles of the NiO_x (left) and PEDOT:PSS (right) layers.

determined the Fermi levels of the NiO_x layer[33], finding a value of approximately 5.1 eV, slightly higher than that (5.0 eV) of the PEDOT:PSS layer.

We also measured the water contact angles of the NiO_x layer and compared these outcomes with those of the reference PEDOT:PSS layer, as shown in Fig. 1c. The observed water contact angles were 16.1° ± 2.8° for the NiO_x layer and 13.4° ± 1.4° for the PEDOT:PSS layer, indicating that the NiO_x surface is more hydrophobic than the PEDOT:PSS layer. Thus, the relatively non-wetting NiO_x surface may improve the film formation of the active perovskite layer and facilitate uniform and continuous perovskite film morphologies with large crystalline domains[34,35].

Next, we examined the effects of the NiO_x and PEDOT:PSS layers on the formation of a light harvester, in this case a perovskite layer ($CH_3NH_3PbI_3$, $MAPbI_3$). Here, the perovskite layers were prepared using a toluene-assisted rapid-crystalline technique[36], to attain a uniform, continuous, flat, and full-coverage film, as mentioned in the "Experimental section". The thickness of the perovskite layer was fixed at 250 nm in all layers and devices in this study, as the device performance of a perovskite photodiode can be influenced by the perovskite film thickness[37]. To compare the film quality levels of the fabricated perovskite layers on the NiO_x and PEDOT:PSS underlying layers as HTLs, the surface morphologies of the perovskite films on the NiO_x and PEDOT:PSS HTLs were characterised by scanning electron microscopy (SEM). Figure 2a,b show surface SEM images of the $CH_3NH_3PbI_3$ perovskite layers on the NiO_x and PEDOT:PSS HTLs, respectively. Notably, the grain size (≈ 254 nm) of the perovskite film on the NiO_x HTL greatly exceeds that (≈ 166 nm) on the PEDOT:PSS HTL. This result verifies that the relatively non-wetting NiO_x surface suppresses perovskite nucleation sites, which facilitates the growth of larger grains[38]. The large grain size of the perovskite film can reduce the recombination rate of the charge carriers due to the decreased charge trap density[34].

As depicted in Fig. 2c, the perovskite films on the NiO_x and PEDOT:PSS HTLs were also characterised by X-ray diffractometry (XRD). Robust and major Bragg peaks were observed at 14.3°, 28.6°, and 32.1°, corresponding to the (110), (220), and (310) planes of the $MAPbI_3$ perovskite film given its orthorhombic crystal structure[34]. On the NiO_x HTL, we observed a slight improvement in the XRD peak intensity levels of the perovskite film

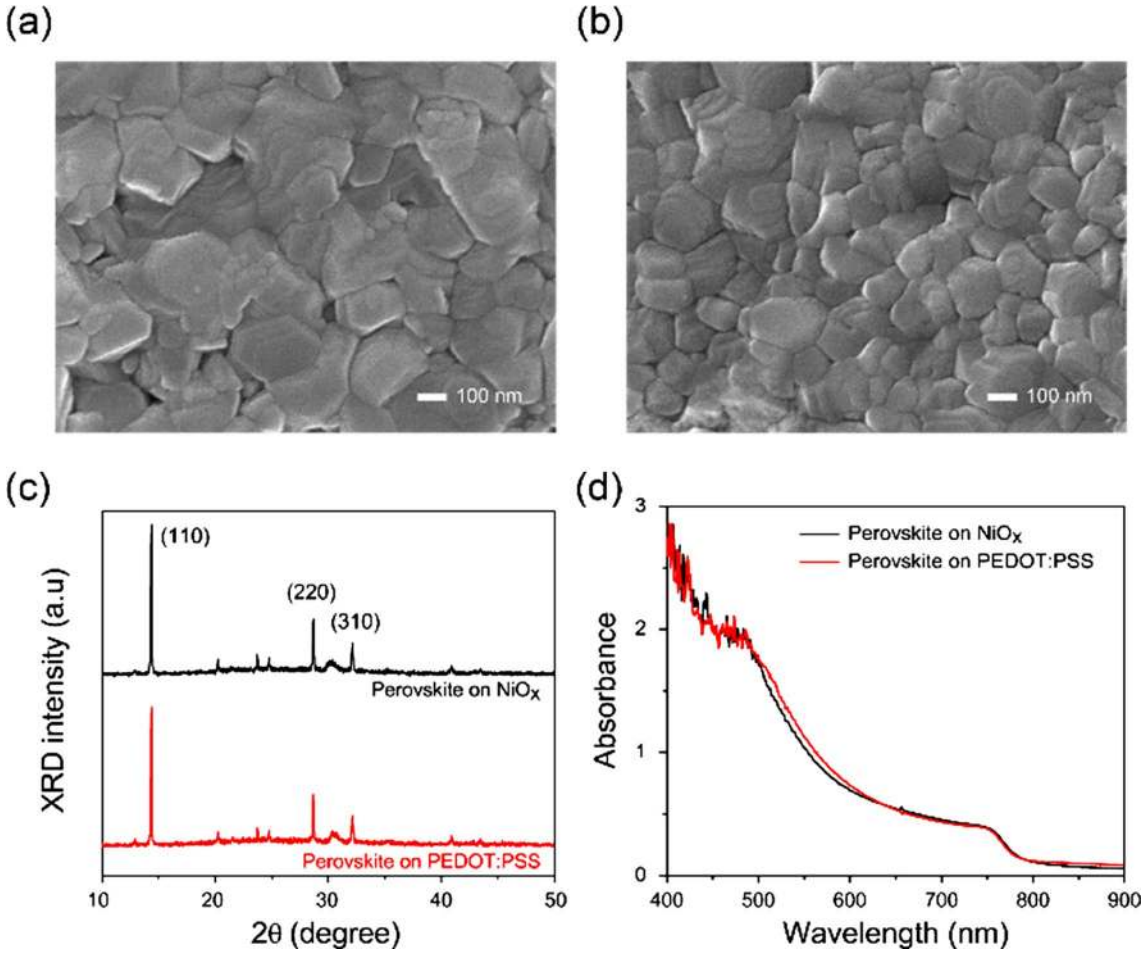

Figure 2. (**a**) SEM image of a perovskite film on the NiO_x layer, (**b**) SEM image of a perovskite film on the PEDOT:PSS layer, (**c**) XRD spectra of the perovskite films on the NiO_x and PEDOT:PSS HTLs, and (**d**) optical absorbance spectra of the perovskite films on the NiO_x and PEDOT:PSS HTLs.

as compared to those on the PEDOT:PSS HTL, also implying the larger grains with high crystallinity of the perovskite film. Note that there was no significant change in the XRD peak ratios, implying that the different HTLs did not cause any substantial change in the crystal orientations of the perovskite films. Figure 2d shows the optical absorption spectra of the perovskite films on the NiO_x and PEDOT:PSS HTLs. We observed that the absorption spectra of the perovskite layers in both cases on the HTLs were nearly identical to each other[34]. It was also noted that the optical transmittance levels of the NiO_x layer are comparable but slightly lower in the visible range compared to those of the PEDOT:PSS layer (Fig. S1).

Next, in order to examine the effects of the NiO_x and PEDOT:PSS HTLs on the surface roughness and energy level of the perovskite layer, AFM and KPFM were used to characterise the perovskite layers on the NiO_x and PEDOT:PSS HTLs. Figures 3a and b show the results of observations of the AFM topologies and the KPFM surface potential maps of the perovskite film on the NiO_x HTL, respectively. For comparison, AFM images and KPFM surface potential maps of the perovskite film on the PEDOT:PSS HTL are shown in Fig. S2. The roughness values of the perovskite films on the NiO_x and PEDOT:PSS HTLs were approximately 8.5 and 9.7 nm, respectively. These results indicate that the active $MAPbI_3$ perovskite layer formed on the NiO_x HTL is more continuous, flat, and uniform than that on the PEDOT:PSS HTL. We also determined the Fermi levels of the perovskite layers on the HTLs using the obtained surface potentials[33], finding that they were approximately 5.1 eV. It is noted that the Fermi level of the NiO_x HTL is closer to that of the perovskite film as compared to that of the PEDOT:PSS HTL. Thus, we considered that the interface quality and affinity between the perovskite layer and the NiO_x HTL are better than those between the perovskite layer and the PEDOT:PSS HTL due to the good crystallinity with large grains, low surface roughness, and a small difference in the Fermi level of the perovskite layer on the NiO_x layer, all of which may promote the performance of perovskite photodiodes[39,40].

Subsequently, we investigated the device performance of a self-powered perovskite photodiode. A schematic illustration of the self-powered perovskite photodiode is presented in Fig. 4a. In the structure, ITO is used as the anode material, NiO_x serves as the HTL, the perovskite layer ($CH_3NH_3PbI_3$) functions as the active layer, phenyl-C61-butyric acid methyl ester ($PCBM_{60}$) and ZnO NPs form the ETLs, bathocuproine (BCP) is used as a buffer layer for a reduction of the nonradiative recombination of excitons, and Al is utilised as the cathode (for details, see the "Experimental section").

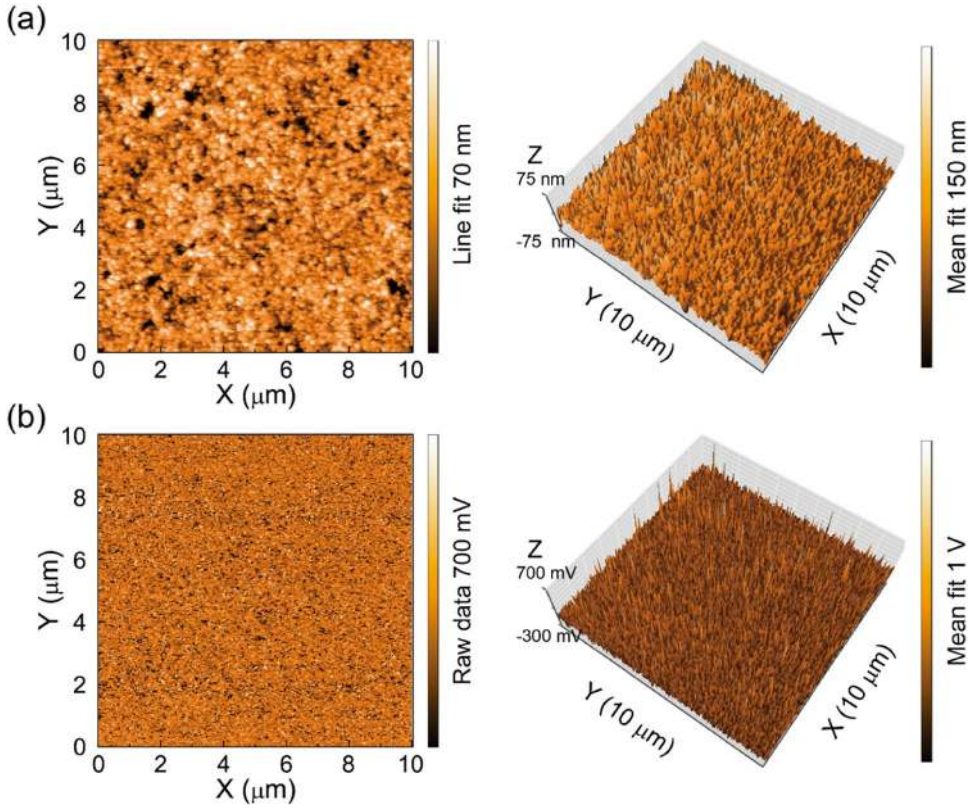

Figure 3. (**a**) AFM image of the perovskite film on the NiO_x HTL (left) with a three-dimensional plot (right) of the perovskite film, and (**b**) KPFM image of the perovskite film on the NiO_x HTL (left) with a three-dimensional plot (right).

Figure 4b shows the energy band diagram of a photodiode with NiO_x or PEDOT:PSS as the HTL. As shown in the fig., it is clear that the NiO_x HTL has a higher valence band maximum (VBM) value (5.3 eV) compared to that (5.2 eV) of the PEDOT:PSS HTL[41,42]. Thus, the NiO_x HTL provides a more favourable alignment of the energy level with respect to the VBM of the perovskite active layer. The high value of the VBM of the NiO_x HTL would decrease the energy barrier, which may in turn increase the build-in potential (V_{bi}) and facilitate improved hole transportation, consequently leading to a larger value of the open-circuit voltage (V_{oc})[24,34,41]. In order to estimate the PV characteristics of the fabricated self-powered perovskite photodiodes, the photocurrent density–voltage (J–V) characteristics of the photodiodes were measured under the AM1.5G illumination source. Figure 4c shows the observed J–V characteristics of the sample perovskite photodiode with the NiO_x HTL (hereafter, the sample device) and of the reference photodiode with the PEDOT:PSS HTL (hereafter, the reference device). The estimated PCE value from the J–V curve was 13% in the sample device with an open-circuit voltage V_{OC} of 1.03 V, a short-circuit current density (J_{SC}) of 21 mA cm^{-2}, and a fill factor (FF) of 61%; the PCE in this case is much higher than the PCE value of 8% in the reference device with $V_{oc} = 0.95$ V, $J_{sc} = 19$ mA cm^{-2}, and $FF = 45\%$. These PV results are consistent with previous results for perovskite PV cells[26,43,44]. Thus, it is obvious that the perovskite photodiodes based on the NiO_x HTL exhibit improved PV performance. Note that the increased V_{oc} value of the sample device is mainly due to the high VBM of the NiO_x HTL, which implies an increase in the built-in potential[29]. We also took measurements via forward and backward scans of the photodiode devices studied here (Fig. S3) to augment our discussion of the hysteresis in the J–V scans of the perovskite devices[45–47]. We calculated the hysteresis index (HI) using the relationship of $HI = \frac{J_{RS}(0.8V_{oc}) - J_{FS}(0.8V_{oc}))}{J_{RS}(0.8V_{0c})}$, where $J_{RS}(0.8V_{OC})$ and $J_{FS}(0.8V_{OC})$ represent the photocurrent densities at a bias voltage of $0.8\,V_{OC}$ for the reverse and forward scans, respectively[47]. The estimated values of HI for the photodiodes with the NiO_x and PEDOT:PSS HTLs are 0.06 and 0.60, respectively, which indicates that the sample photodiode with the NiO_x HTL shows negligible hysteresis. Thus, the much smaller value of HI for the photodiode with the NiO_x HTL than for that with the PEDOT:PSS HTL is mainly owing to the high crystallinity of the perovskite layer and rapid charge extraction by the NiO_x HTL[45–47].

At this point, we focus our attention on the photodiode performance of the sample device fabricated with NiO_x. Figure 4d shows the current density as a function of the bias voltage (J–V) at different input power levels (0 – 349 mW cm^{-2}) of incident laser light having a wavelength of $\lambda = 532$nm. We swept the voltage from − 1.0 to + 2.0 V and measured the current density J. Both the forward and reverse current density levels increase gradually as the input power of the incident light increases.

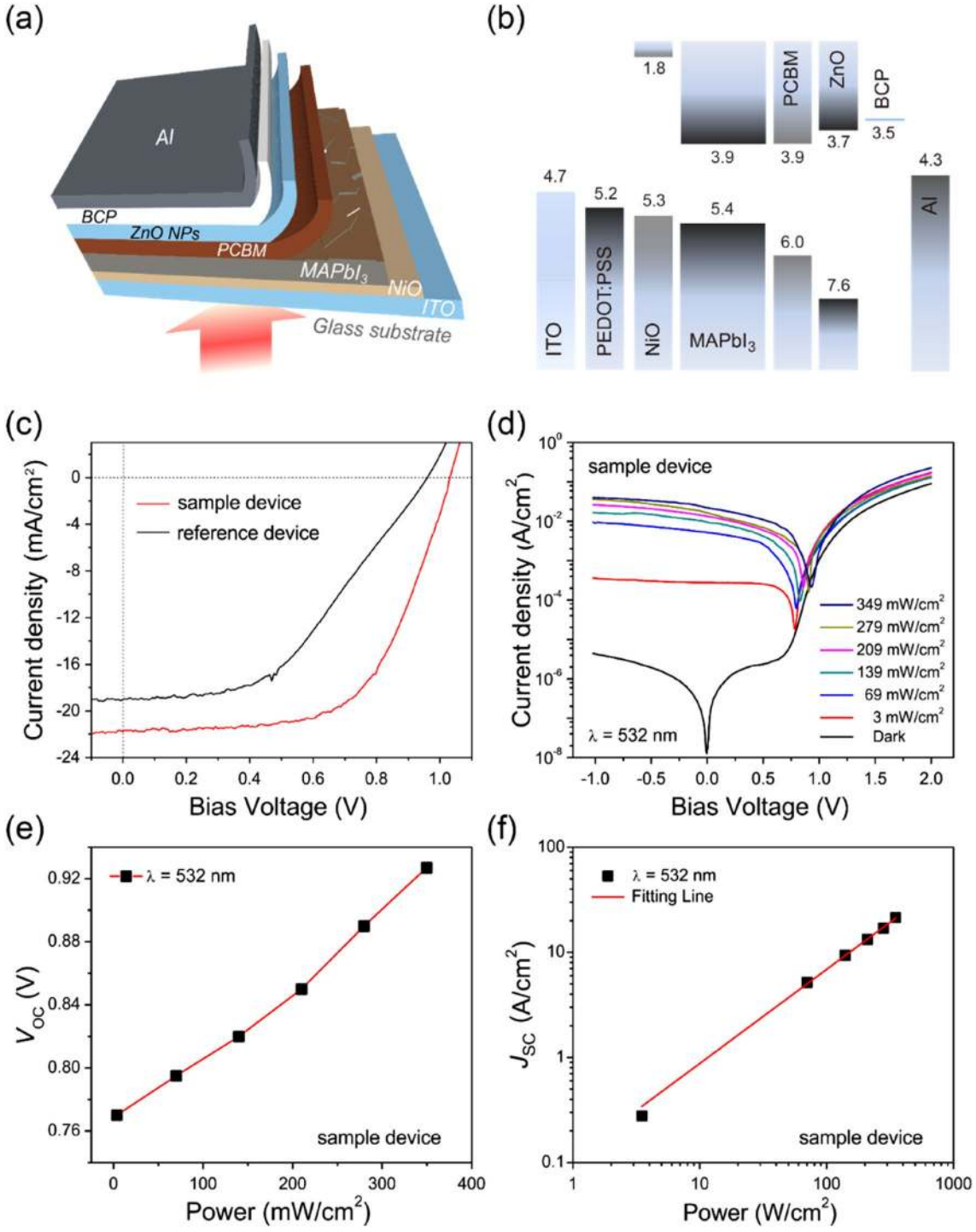

Figure 4. (**a**) Schematic diagram of a self-powered perovskite photodiode with NiO_x as an electron-blocking and HTL, (**b**) energy band diagram of the self-powered perovskite photodiode, (**c**) photovoltaic measurements of the perovskite photodiodes under an AM1.5G illumination source, (**d**) photocurrent density of the perovskite photodiode with the NiO_x HTL as a function of the bias voltage for several different intensity levels of incident light with a wavelength of 532 nm, (**e**) open-circuit voltage (V_{oc}) of the photodiode with the NiO_x HTL as a function of the input power of the incident laser light, and (**f**) short-circuit current density (J_{sc}) of the photodiode with the NiO_x HTL as a function of the input power of incident light (532 nm) at zero bias voltage.

Meanwhile, asymmetric electrodes (ITO and Al) of the fabricated perovskite photodiodes generate the built-in potential V_{bi} that drives the operation of the photodiodes, even under zero external bias voltage, *i.e.*, a self-powered condition. Figure 4e,f show the variations in V_{oc} and the short-circuit current density J_{sc}, as a function of the input power of the incident laser light (532 nm), respectively, for the sample device with NiO_x. As shown

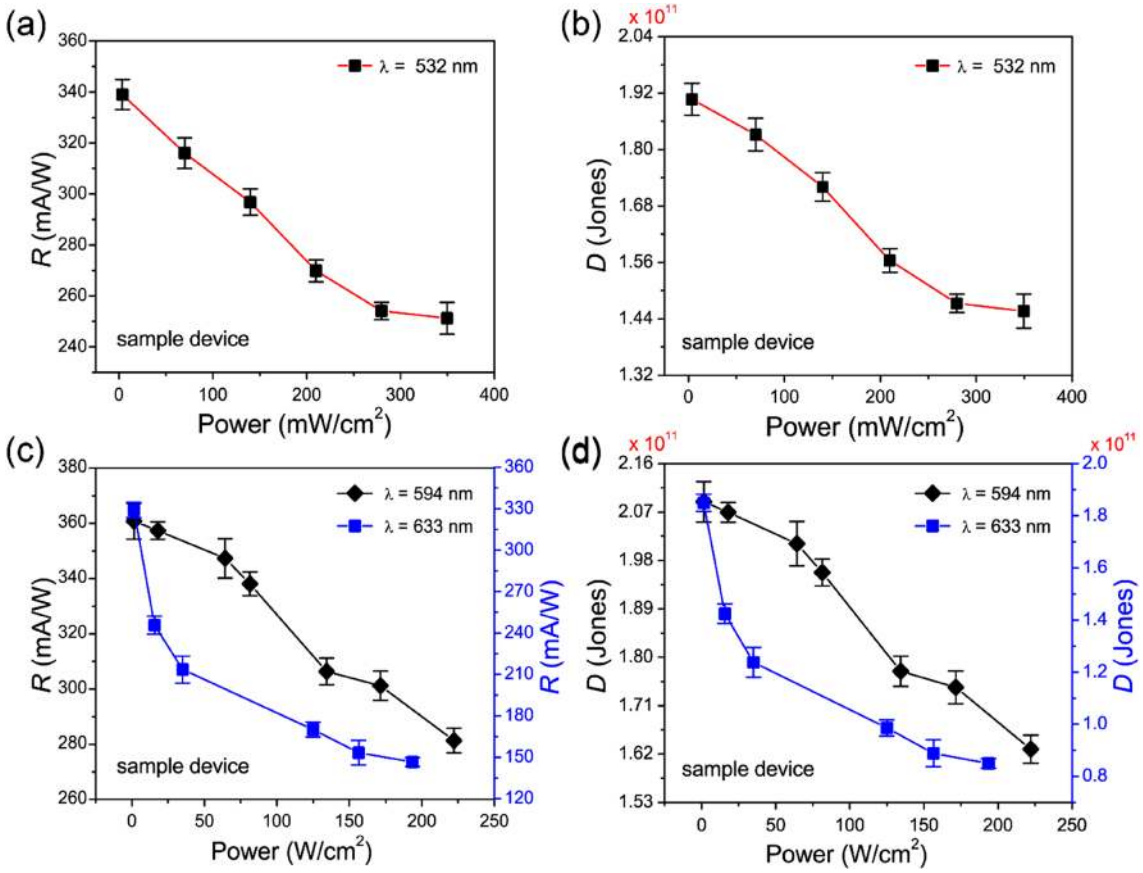

Figure 5. Responsivity *R* (**a**) and detectivity *D,* (**b**) of the perovskite photodiode with the NiO_x HTL as a function of the input power of incident light (532 nm) at zero bias voltage, and comparison of the responsivity *R,* (**c**) and detectivity *D,* (**d**) of the photodiode as a function of the input power of incident light with different wavelengths (594 and 633 nm) at zero bias voltage.

in the figures, V_{oc} and J_{sc} increase gradually to 0.92 V and 23 mA cm^{-2}, respectively, as the input power of the incident light increases from 0 to 349 mW cm^{-2}. Here, J_{sc} is increased considerably, likely due to the large number of photo-excited charge carriers separated under the high built-in potential V_{bi}. The V_{oc} and J_{sc} values for the reference device with PEDOT:PSS are also correspondingly shown in Figs. S4 and S5. As compared in these figures, higher values of V_{oc} and J_{sc} for the sample device were clearly observed. This result stems from the better electron-blocking and hole-transporting capabilities of the NiO_x HTL. It is also noted that J_{sc} reveals linear dependence on the input power of the incident light (Figs. 4f and S8). This dependence of J_{sc} can be analysed using the following relationship[48],

$$J_{sc} = cP^{\theta}, \tag{1}$$

where *c*, *P*, and θ are a proportional constant, the input power intensity of the incident laser light, and the power-law index, respectively. With best-fit parameters, the obtained value of θ for the sample device with NiO_x is 0.89, which is close to 1.0 for an ideal photodiode with a low trap state junction and which is noticeably higher than that ($\theta = 0.69$) for the reference device with PEDOT:PSS (Fig. S5). Such a relatively large θ value for the sample device indicates that a small number of trap states exist in the perovskite layer on the NiO_x HTL, which is valuable for the realisation of high photo-sensing ability through the efficient collection of a large number of photo-excited charge carriers.

Next, to evaluate *R* and *D* of the perovskite photodiode at zero bias voltage ($V_{bias} = 0$ V, self-powered condition), we used the following relationship[49],

$$R = J_{PH}/PA, \tag{2}$$

where J_{PH} is the net photocurrent density $\left(J_{PH} = J_{light} - J_{dark}\right)$ and *A* denotes the illuminating junction area of the photodiode for the incident laser light. Figure 5a shows the *R* value, estimated from the current density data (shown in Fig. 4d), as a function of the input power of incident laser light (532 nm) for the sample device. The highest estimated *R* value of the sample device is 340 mA W^{-1} at zero bias voltage (self-powered), which is much higher as compared to previously reported values, mainly due to the efficient suppression of the dark leakage current. Moreover, the value of *R* increases to 440 mA W^{-1} when the bias voltage $V_{bias} = -1.0$ V. We also estimated the detectivity *D* value of the sample device using the following relationship[50],

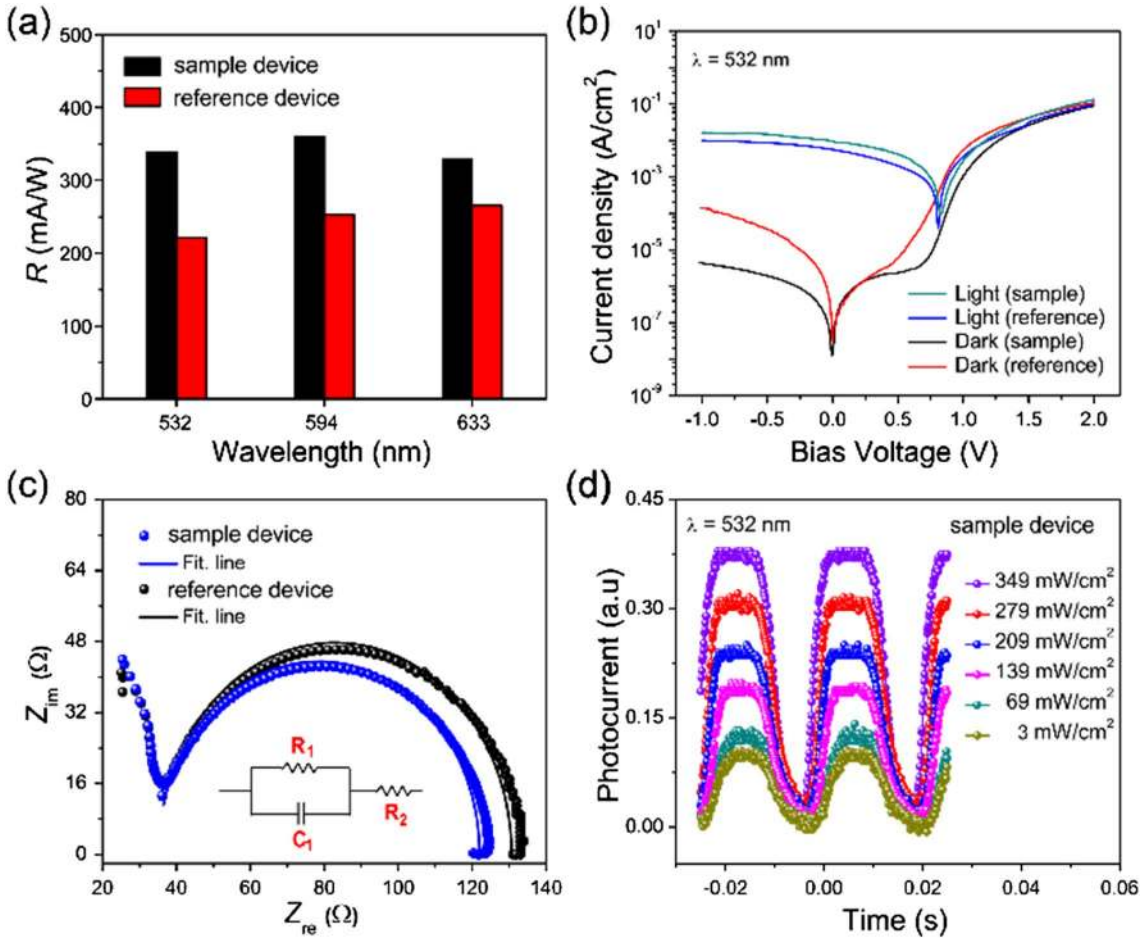

Figure 6. (**a**) Comparison of *R* values for the perovskite photodiodes with NiO_x and PEDOT:PSS as HTLs, (**b**) dark- and photo-current densities of the photodiodes with NiO_x and PEDOT:PSS as HTLs under illumination of incident light (532 nm), (**c**) impedance spectra (IS) of the photodiodes with the NiO_x or PEDOT:PSS HTLs at zero bias voltage, and (**d**) temporal photoresponses of the photodiode with the NiO_x HTL for several input power levels of incident light (532 nm) at zero bias voltage when turning the incident light on and off.

$$D = \frac{R}{\sqrt{2qJ_{dark}}}, \tag{3}$$

where *q* denotes the charge of the electron. Figure 5b shows the *D* values obtained for several input power levels of incident laser light (532 nm). The highest estimated *D* value of the sample device with NiO_x is approximately 1.9×10^{11} Jones, which is also much higher than earlier values reported in the literature.

Additionally, we measured the *R* and *D* values of the sample device with NiO_x with incident laser light at wavelengths of 594 and 633 nm to quantify the wavelength selectivity of the photodiode, as shown in Fig. 5c,d, respectively. In this case, we also obtained high corresponding *R* values of 360 and 330 mA W^{-1} with improved *D* values of 2.08×10^{11} and 1.8×10^{11} Jones under incident laser light illumination with wavelengths of 594 and 633 nm, respectively, at zero bias voltage. These results clearly demonstrate the highly efficient self-powered operation of the perovskite photodiode studied here.

Figure 6a shows comparisons of the *R* values obtained from the sample and reference devices in three incident light with different wavelengths. Clear differences were noted in *R* values, and the *R* value is enhanced from 240 to 360 mA W^{-1} at 594 nm when NiO_x is introduced to replace the conventional PEDOT:PSS as the HTL. This outcome provides clear evidence that the sample device based on the NiO_x HTL exhibits superior responsivity *R* relative to the reference device based on the conventional PEDOT:PSS HTL. We also measured the stability of the photodiodes studied here with the NiO_x and PEDOT:PSS HTLs (Fig. S6). As shown in the figure, the device with NiO_x is much more stable as compared to that with PEDOT:PSS[25,51]. Thus, it is clear that our self-powered perovskite-based photodiode with NiO_x is promising for highly sensitive photodiodes requiring low energy consumption levels.

Discussion

In order to understand the cause of such high responsivity of the sample device with NiO_x, the dark and photo *J–V* characteristics were compared and analysed, as shown in Fig. 6b. In this figure, we also compare the *J–V* curves of the reference device with PEDOT:PSS. In a dark condition, we observed clear diode behaviour with a

high rectification ratio of 2.0×10^4 for the sample device. This rectification ratio is nearly 27 times higher than that (7.5×10^2) for the reference device. Moreover, the sample device with NiO_x clearly shows relatively low leakage current compared to the reference device with PEDOT:PSS. The dark current density is suppressed in the sample device to 7.84×10^{-6} mA cm^{-2}, a much smaller value as compared to that (2.84×10^{-5} mA cm^{-2}) of the reference device at zero bias voltage. This reduction in the dark current density confirms the low leakage current in the perovskite photodiode with NiO_x[27]. Thus, it is clear that the perovskite photodiode based on the NiO_x HTL exhibits much better diode characteristics than the reference device with the conventional PEDOT:PSS HTL. Further, the sample device shows higher photocurrent density levels under incident laser light in both the forward and reverse regions as compared to the results of the reference device. The photocurrent density of the sample device increases to 7.5 mA cm^{-2} under incident laser light (532 nm) with an input power of 349 mW cm^{-2} at zero bias voltage. Therefore, we considered that the relatively low leakage current in the dark and the increased photocurrent outcomes of the sample device with NiO_x may promote the improved device performance through the realisation of a leakage-free photodiode.

To clarify the remarkable effect of the NiO_x HTL on the high responsivity of the perovskite photodiode, the dark current flows of the devices (Fig. 6b) are analysed using the following relationship for the Shockley diode in a single-junction device[52],

$$J = J_0\left[\exp\left(\frac{qV}{nKT}\right) - 1\right], \tag{4}$$

where J_0, n, K, and T represent the saturation current density, ideality factor, Boltzmann's constant, and temperature, respectively. For an ideal diode (p–n junction), the ideality factor n is expected to be equal to 1.0 without charge carrier trapping[53]. Thus, the ideality factor n can be a key parameter to estimate the suppression of the recombination rate in perovskite photodiodes. From the analyses of the dark currents, the estimated values of ns are 1.1 and 1.7 for the sample and reference devices, respectively. The smaller value of n for the sample device as compared to that for the reference device stems from the reduced number of monomolecular recombinations[53]. To verify this reduction of recombinations, we also estimated the recombination resistance R_{rec} for the charge carriers using the following relationship[54],

$$R_{rec} = \frac{V_e}{J_{sc}}\left(e^{q\left(\frac{V_{oc}-V_e-B}{nKT}\right)}\right), \tag{5}$$

where V_e, and R_s represent the effective voltage, the minimum voltage used to extract n from the J–V curves, and the series resistance, respectively. Based on the above relationship, we obtained a higher value of R_{rec} ($\approx 105\Omega$) for the sample device with NiO_x as compared to that ($\approx 79\Omega$) for the reference device with PEDOT:PSS. Thus, the higher R_{rec} for the sample device verifies higher resistivity to carrier recombinations in the photodiode with the NiO_x HTL[54,55].

To clarify and examine the defect states and trap recombination at the HTL/perovskite interface, the space-charge limited current model is employed. The trap-state density (n_{trap}) can be calculated using the following relationship[56],

$$n_{trap} = \frac{2\varepsilon\varepsilon_o V_{TFL}}{eL^2}, \tag{6}$$

where ε, ε_0, V_{TFL}, e, and L correspondingly represent the relative dielectric constant of perovskite, the dielectric constant of a vacuum, the trap-filling limited voltage, the elementary charge, and the thickness of the perovskite film. The value of V_{TFL} can be derived from the J–V characteristics of reference and sample photodiode devices in a dark condition (Fig. S7). The V_{TFL} values of the devices with the NiO_x and PEDOT:PSS HTLs are 0.42 and 0.74 V, respectively. Thus, the estimated n_{trap} values of the devices are 1.83×10^{15} cm^{-3} for the reference device with the PEDOT:PSS HTL and 1.12×10^{15} cm^{-3} for the sample device with the NiO_x HTL, clearly demonstrating fewer trap recombinations at the NiO_x/perovskite interface[20,57].

Next, the reduction of charge recombination of the sample device was analysed further on the basis of the open-circuit voltage V_{oc} because all of the photo-excited charge carriers will recombine within the device at the end at the open-circuit condition[36,58]. By linear least squares fitting of the V_{oc} data (Fig. 4e), slopes of $1.2K_BT/q$ and $1.4K_BT/q$ were attained for the sample and reference devices, respectively. In principle, when the slope is equal to $1.0K_BT/q$, the device operates without trapping charge carriers or is governed by bimolecular recombinations, and the active layer is considered as having recombinations free of electrons and holes; when the slope exceeds $1.0K_BT/q$, monomolecular Shockley–Read–Hall (SRH) recombinations are involved[53]. Thus, our NiO_x-based sample device exhibits a smaller slope of $1.2K_BT/q$ than that ($1.4K_BT/q$) of the reference device, verifying that the NiO_x-based device can efficiently reduce monomolecular recombinations with less charge carrier trapping, contributing to the improvement of the device performance[59].

Further, we estimated V_{bi} of the perovskite photodiode using the relationship ($V_{bi} = {}^{-nK_BT}/_{q}(\ln J_0)$) of the diode model[60]. The estimated value of V_{bi} is $\approx$ 0.52V for the sample device with NiO_x, while the value of V_{bi} is $\approx$ 0.36 V for the reference device with PEDOT:PSS. Such a high V_{bi} value of the sample device is a direct signature of the improved charge-selecting properties of the NiO_x HTL. Thus, it is clear that the hole-selecting capability of NiO_x is much greater than that of PEDOT:PSS, causing the high responsivity of the self-powered perovskite photodiode to be greater with NiO_x[29].

Next, to gain a deeper understanding of the charge transfer in the perovskite photodiodes based on distinct HTLs, impedance spectroscopy (IS) measurements were taken for the photodiodes in the dark. Figure 6c shows

Nyquist plots from IS data for the photodiodes with NiO_x and PEDOT:PSS at zero bias voltage. We observed clear semicircles that distinguish the intermediate-frequency (f) regions for both photodiodes. These are linked to the charge transfer at the HTL/perovskite/ETL interfaces, primarily owing to recombinations. From the fitting of the IS data, the capacitance (C_1), parallel resistance (R_1), and series resistance (R_2) values of the photodiodes with NiO_x and PEDOT:PSS were deduced. The equivalent circuit diagram is shown in the inset figure. The obtained values of C_1, R_1, and R_2 are correspondingly 3.87 nF, 87.04 Ω and 34.94 Ω for the sample device with NiO_x and are 3.90 nF, 95.48 Ω and 35.14 Ω for the reference device with PEDOT:PSS. The C_1 and R_2 values of the sample device are slightly lower than those of the reference device, indicating fewer surface trap state charges with less charge accumulation at the interface between the perovskite layer and the NiO_x HTL compared to the PEDOT:PSS HTL. Moreover, the R_1 value of the sample device is clearly lower than that of the reference device. This low R_1 of the NiO_x-based perovskite photodiode can be attributed to the low interfacial charge transfer resistance at the perovskite/NiO_x interface. The smaller value of R_1 also implies faster hole transport at the NiO_x/perovskite interface compared to that at the PEDOT:PSS/perovskite interface.

Next, we also measured the temporal responses of the sample device with NiO_x as the HTL at various input power levels ($P = 3$, 69, 139, 209, 279, and 349 mW cm^{-2}) while turning the incident laser light (532 nm) on and off (Fig. 6d). The rapid rise (τ_r) and decay (τ_d) response times of the sample device were found to be $\tau_r \approx 0.9$ and $\tau_d \approx 1.8$ ms, respectively, at zero bias voltage. For comparison, we also measured the photoresponse of the reference device (Fig. S8). From the comparison, it was found that the photoresponse of the sample device is much faster than that ($\tau_r \approx 3$, $\tau_d \approx 10$ ms) of the reference device. Thus, it is clearly shown that the NiO_x HTL is a key component required to realise a fast self-powered perovskite-based photodiode.

Next, the *EQE*s of the perovskite photodiodes were also estimated from their R values using the following relationship[61],

$$EQE = R\frac{hc}{e\lambda}, \tag{7}$$

where h and c correspondingly denote the Planck constant $\left(6.62 \times 10^{-34}\,\mathrm{J\,s}\right)$ and the speed of light $\left(3.8 \times 10^{8}\,\mathrm{ms^{-1}}\right)$. The estimated *EQE* values are 76.5% and 61% for the sample device with NiO_x and the reference device with PEDOT:PSS, respectively, at a wavelength of 532 nm. As expected, the *EQE* value of the sample device with NiO_x is much higher than that of the reference device with PEDOT:PSS. This high *EQE* value for the sample device is the result of the improved charge-selecting properties as well as the improved exciton dissociation at the perovskite/HTL interface with the help of the high built-in electric field in the heterostructure. In order to confirm the estimated *EQE* values, we also measured the *EQE* spectra using an incident photon-to-current collection efficiency (IPCE) system, as shown in Fig. 7a. The measured *EQE* values from IPCE measurements were 76% and 60% for the sample and reference devices, respectively, at the wavelength of 532 nm, which are nearly identical to those estimated from the R values. For further comparison with other wavelengths, Fig. 7b shows the high *EQE* values estimated from both R and IPCE measurements of the sample device with NiO_x, verifying the close correspondence of these values and supporting the high device performance of the perovskite photodiode with the NiO_x HTL.

Finally, the improved responsivity R value of our sample device is compared with those in previous reports to emphasise the novelty of the results with the electron-blocking NiO_x HTL (see Fig. 7c and Table S1)[12,48,62–71]. We also compared D with other reported values in Table S1, as shown in Fig. 7d[50,65,68,71–77]. It is clear from these figures that R and D of our photodiode with NiO_x in this study are much higher compared to those reported previously. These findings overall show that the interface quality and recombination activities in perovskite photodiodes are mainly influenced by the electron-blocking NiO_x HTL, which will surely provide a platform for further improvements in the performance of photodiodes coupled with excellent charge-selecting layers.

Conclusions

In summary, we designed a self-powered hybrid organic–inorganic perovskite photodiode with an effective and capable electron-blocking hole-transport NiO_x layer. We used NiO_x as the HTL in the fabrication of the perovskite photodiode to improve the interface quality by suppressing the dark leakage current reaching to 7.84×10^{-6} mA cm^{-2}. The perovskite photodiode fabricated with NiO_x exhibited better PV performance with a PCE of 13% as compared to the photodiode with conventional PEDOT:PSS. A remarkably high responsivity R value of 360 mA W^{-1} with detectivity $D = 2.08 \times 10^{11}$ Jones and $EQE = 76.5\%$ for the self-powered perovskite photodiode with the NiO_x HTL was noted under incident laser light with a wavelength of 594 nm at zero bias voltage. Further, the performance capabilities of the perovskite photodiode were estimated at different bias voltages; the value of R increased gradually to 428 mA W^{-1} with $D = 3.6 \times 10^{11}$ Jones and $EQE = 77\%$ at a bias voltage of $V_{bias} = -1$ V. Based on the diode model, we deduced an ideality factor of 1.1 and a high built-in potential value of $V_{bi} \approx 0.52$V for the photodiode with the NiO_x HTL, thus providing direct evidence of the improvement of the charge-selecting characteristics of the NiO_x layer. Furthermore, we observed fast rise and decay times of approximately 0.9 to 1.8 ms, respectively, for the perovskite photodiode with the NiO_x HTL at zero bias voltage, values which are much faster than those of the reference photodiode with the conventional PEDOT:PSS HTL. Therefore, the self-powered perovskite photodiode studied here opens up an opportunity for applications of hybrid perovskite heterostructures with the electron-blocking NiO_x HTL in highly sensitive light-detecting optoelectronic devices that consume low amounts of energy, such as optical sensors, waveguide-integrated photodiodes, and/or nano-photodetectors.

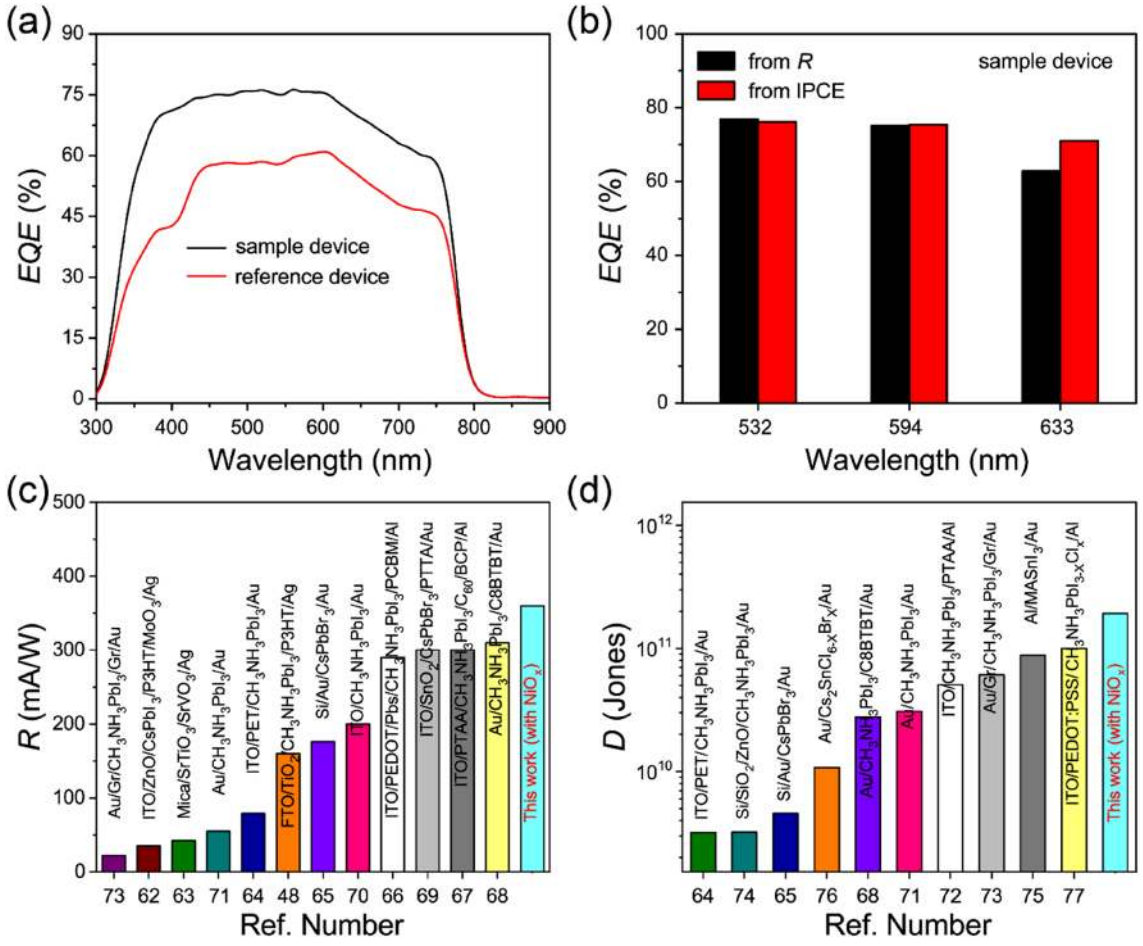

Figure 7. (**a**) *EQE* spectra as a function of the wavelength for the perovskite photodiodes with NiO_x or PEDOT:PSS as HTLs, (**b**) comparison of measured (from IPCE) and estimated (from *R*) values of the *EQE*s at zero bias voltage for three different wavelengths of incident light, and comparisons of the *R* (**c**) and *D* (**d**) values of several previously reported perovskite photodiodes.

Experimental section

Materials. All materials (organic and inorganic) used here were obtained from commercial sources and were used without any extra purification steps. The materials of anhydrous gamma-butyrolactone (GBL, 99%), anhydrous dimethyl sulfoxide (DMSO, 99%), anhydrous chlorobenzene (CB, 99.9%), and nickel (II) nitrate hexahydrate ($Ni(NO_3)_2{\cdot}6H_2O$) (99.998%) were purchased from Sigma-Aldrich. Isopropyl alcohol (IPA, 99.7%) and ethylene glycol ($C_2H_6O_2$, 99%) were purchased from Daejung. Lead (II) iodide (PbI_2, 99%) was purchased from Alfa Aesar and the methyl-ammonium iodide (MAI, > 99%) used here was from Greatcell Solar. The suspension of ZnO NPs was purchased from Avantama (N-10). Other chemicals, specifically poly (3, 4-ethylene dioxythiophene) polystyrene sulfonate (PEDOT:PSS), were from H. C. Starck (Clevios PVP AI 4083). Phenyl-C61-butyric acid methyl ester ($PCBM_{60}$) and bathocuproine (BCP, 98%) were purchased correspondingly from Nano-C and TCI.

Device fabrication and characterisation. Glass substrates coated with an indium tin oxide (ITO) layer (80 nm, 30 Ω/square) were sequentially put into ethanol, a detergent, and deionised water (DI) in an ultrasonic bath (20 min for each step) to clean them. Subsequently, the ITO substrates were dried with N_2 and treated with atmospheric O_2 plasma for 2 min. A NiO_x precursor solution was prepared by dissolving $Ni(NO_3)_2$ $6H_2O$ (≈ 0.029 g) in a mixed solvent of ethylene glycol and IPA at a 3:2 volume ratio.

To form the HTLs of NiO_x (40 nm) and PEDOT:PSS (40 nm), the prepared solutions were spin-coated onto ITO substrates at 3000 rpm for 40 s and at 4000 rpm for 35 s, respectively. For NiO_x, the coated precursor layer was annealed at 70 °C for 1 min and then at 300 °C for 1 h, while for PEDOT:PSS, the coated layer was annealed at 120 °C for 30 min. To make the perovskite precursor solution, a mixture of MAI and PbI_2 at a 1:1 molar ratio was dissolved in a mixed solvent of GBL and DMSO at a 7:3 volume ratio. The precursor solution was stirred overnight at 60 °C. The perovskite precursor solution (50 µl) was spin-coated at 1000 rpm for 10 s and then at 3000 rpm for 25 s to obtain the desired thickness of 250 nm onto the NiO_x and PEDOT:PSS layers. During the spinning process, an anti-solvent (toluene ~ 150 µl) was poured onto the precursor layer at 17 s. The perovskite precursor layer was then annealed at 100 °C for 20 min. For the ETL, a 20 mg/ml of $PCBM_{60}$ solution, dissolved

in CB, was spin-coated at 1500 rpm for 60 s onto the perovskite layer. A dispersion of ZnO NPs mixed with IPA (7:3) was then spin-coated at 1000 rpm for 10 s and at 4000 rpm for 40 s onto the $PCBM_{60}$ layer. Finally, BCP (12 nm) and Al (70 nm) were deposited onto the ZnO NP layer using a thermal evaporation system. Thus, the device structure of the sample photodiode was [ITO/NiO_x/$CH_3NH_3PbI_3$/$PCBM_{60}$/ZnO NPs/BCP/Al]. The active area of the fabricated devices was 6 mm^2 in size.

Film and device characterisation. The water contact angles of the fabricated NiO_x and PEDOT:PSS layers were measured using a contact angle meter (Phoenix 300 Touch, Surface Electro Optics). The fabricated perovskite film was characterised using a field emission scanning electron microscope (SEM, Model JSM-6700F, JEOL Co.) to analyse the surface morphology. To investigate the surface roughness and surface potential of the organic and inorganic functional layers, atomic force microscopy (AFM) and Kelvin probe force microscopy (KPFM, FlexAFM, Nanosurf AG) were used. To measure the surface potential, a Pt/Ir-coated silicon tip (resonance frequency = 87 kHz and a force constant = 3.9 Nm^{-1}, NanoWorld, Inc.) was used while applying AC voltage of 1 V at a frequency of 18 kHz.

An X-ray diffractometer (XRD-Rigaku D/Max 2200, $\lambda = 0.154$ nm) was used to check the crystallinity of the perovskite layers on the NiO_x and PEDOT:PSS layers. To estimate the optical absorption spectra of the perovskite layers, a UV–visible spectroscopy system (8453, Agilent) was employed. The photocurrent versus bias voltage (*J–V*) characteristics were measured using a source meter (2400, Keithley) under illumination of incident laser light with several different wavelengths and were calibrated using a reference commercial silicon photodiode (THORLABS-PDA10A2) (see Fig. S9). The PV performance of the fabricated photodiode was measured under an illumination intensity of 100 mW cm^{-2} generated by an AM1.5 light source (Newport, 96,000 Solar Simulator) and calibrated using a reference cell (Bunkoh-keiki, BS-520). Impedance spectroscopy (IS) measurement of the photodiode was performed in the dark using an impedance analyser (HP 4192A) with an AC oscillating amplitude of 100 mV (RMS) to maintain the linearity of the response. The *EQE* spectra were also measured using an incident photon-to-current collection efficiency (IPCE) measurement system (IQE-200 EQE/IQE, Newport).

Received: 25 August 2020; Accepted: 2 December 2020
Published online: 08 January 2021

References

1. Zhang, Y. *et al.* Ultrasensitive photodetectors exploiting electrostatic trapping and percolation transport. *Nat. Commun.* **7**, 1–9 (2016).
2. Zhou, Y. *et al.* Thin-film Sb 2 Se 3 photovoltaics with oriented one-dimensional ribbons and benign grain boundaries. *Nat. Photonics* **9**, 409–415 (2015).
3. Haider, G. *et al.* Electrical-polarization-induced ultrahigh responsivity photodetectors based on graphene and graphene quantum dots. *Adv. Funct. Mater.* **26**, 620–628 (2016).
4. Yu, Z. & Aceves-Mijares, M. A ultraviolet-visible-near infrared photodetector using nanocrystalline Si superlattice. *Appl. Phys. Lett.* **95**, 081101 (2009).
5. Ponseca, C. S. Jr. *et al.* Organometal halide perovskite solar cell materials rationalized: ultrafast charge generation, high and microsecond-long balanced mobilities, and slow recombination. *J. Am. Chem. Soc.* **136**, 5189–5192 (2014).
6. Spina, M. *et al.* Ultrasensitive 1D field-effect phototransistors: CH 3 NH 3 PbI 3 nanowire sensitized individual carbon nanotubes. *Nanoscale* **8**, 4888–4893 (2016).
7. Zhu, H. L. *et al.* Achieving high-quality Sn–Pb perovskite films on complementary metal-oxide-semiconductor-compatible metal/silicon substrates for efficient imaging array. *ACS Nano* **13**, 11800–11808 (2019).
8. Zhu, H. L. *et al.* Low-bandgap methylammonium-rubidium cation Sn-Rich perovskites for efficient ultraviolet–visible–near infrared photodetectors. *Adv. Func. Mater.* **28**, 1706068 (2018).
9. Kojima, A., Teshima, K., Shirai, Y. & Miyasaka, T. Organometal halide perovskites as visible-light sensitizers for photovoltaic cells. *J. Am. Chem. Soc.* **131**, 6050–6051 (2009).
10. Liu, M., Johnston, M. B. & Snaith, H. J. Efficient planar heterojunction perovskite solar cells by vapour deposition. *Nature* **501**, 395–398 (2013).
11. Pandey, K. *et al.* High-performance self-powered perovskite photodetector with a rapid photoconductive response. *RSC Ad.* **6**, 105076–105080 (2016).
12. Chen, Z. *et al.* Improving performance of hybrid graphene-perovskite photodetector by a scratch channel. *Adv. Electron. Mater.* **5**, 1900168 (2019).
13. Zhou, H., Mei, J., Xue, M., Song, Z. & Wang, H. High-stability, self-powered perovskite photodetector based on a CH3NH3PbI3/GaN heterojunction with C60 as an electron transport layer. *J. Phys. Chem. C* **121**, 21541–21545 (2017).
14. Hu, L. *et al.* An optimized ultraviolet-a light photodetector with wide-range photoresponse based on ZnS/ZnO biaxial nanobelt. *Adv. Mater.* **24**, 2305–2309 (2012).
15. Bie, Y. Q. *et al.* Self-powered, ultrafast, visible-blind UV detection and optical logical operation based on ZnO/GaN nanoscale p-n junctions. *Adv. Mater.* **23**, 649–653 (2011).
16. Bayan, S., Gogurla, N., Midya, A. & Ray, S. K. White light emission characteristics of two dimensional graphitic carbon nitride and ZnO nanorod hybrid heterojunctions. *Carbon* **108**, 335–342 (2016).
17. Tsai, M.-L. *et al.* Monolayer MoS2 heterojunction solar cells. *ACS Nano* **8**, 8317–8322 (2014).
18. Xia, H.-R., Li, J., Sun, W.-T. & Peng, L.-M. Organohalide lead perovskite based photodetectors with much enhanced performance. *Chem. Commun.* **50**, 13695–13697 (2014).
19. Wang, F. *et al.* Fast photoconductive responses in organometal halide perovskite photodetectors. *ACS Appl. Mater. Interfaces.* **8**, 2840–2846 (2016).
20. Huang, Z. *et al.* A general method: designing a hypocrystalline hydroxide intermediate to achieve ultrasmall and well-dispersed ternary metal oxide for efficient photovoltaic devices. *Adv. Funct. Mater.* **29**, 1904684 (2019).
21. Ouyang, D. *et al.* Strategic synthesis of ultrasmall NiCo2O4 NPs as hole transport layer for highly efficient perovskite solar cells. *Adv. Energy Mater.* **8**, 1702722 (2018).
22. Yang, B. *et al.* Multifunctional synthesis approach of In:CuCrO2 nanoparticles for hole transport layer in high-performance perovskite solar cells. *Adv. Funct. Mater.* **29**, 1902600 (2019).

23. Kaneko, R. *et al.* Perovskite solar cells using surface-modified NiOx nanoparticles as hole transport materials in n-i-p configuration. *Solar RRL* **3**, 1900172 (2019).
24. Jin, Z. *et al.* Modification of NiO x hole transport layer for acceleration of charge extraction in inverted perovskite solar cells. *RSC Adv.* **10**, 12289–12296 (2020).
25. You, J. *et al.* Improved air stability of perovskite solar cells via solution-processed metal oxide transport layers. *Nat. Nanotechnol.* **11**, 75–81 (2016).
26. Wang, K.-C. *et al.* Low-temperature sputtered nickel oxide compact thin film as effective electron blocking layer for mesoscopic NiO/CH3NH3PbI3 perovskite heterojunction solar cells. *ACS Appl. Mater. Interfaces.* **6**, 11851–11858 (2014).
27. Zhu, H. L. *et al.* Room-temperature solution-processed NiO x: PbI2 nanocomposite structures for realizing high-performance perovskite photodetectors. *ACS Nano* **10**, 6808–6815 (2016).
28. Yin, X., Que, M., Xing, Y. & Que, W. High efficiency hysteresis-less inverted planar heterojunction perovskite solar cells with a solution-derived NiO x hole contact layer. *J. Mater. Chem. A* **3**, 24495–24503 (2015).
29. Sajid, S. *et al.* Breakthroughs in NiOx-HTMs towards stable, low-cost and efficient perovskite solar cells. *Nano Energy* **51**, 408–424 (2018).
30. Abdollahi Nejand, B., Ahmadi, V. & Shahverdi, H. R. New physical deposition approach for low cost inorganic hole transport layer in normal architecture of durable perovskite solar cells. *ACS Appl. Mater. Interfaces* **7**, 21807–21818 (2015).
31. Akin, S. *et al.* New strategies for defect passivation in high-efficiency perovskite solar cells. *Adv. Energy Mater.* **10**, 1903090 (2020).
32. Zheng, X. *et al.* Interface modification of sputtered NiO x as the hole-transporting layer for efficient inverted planar perovskite solar cells. *J. Mater. Chem. C* **8**, 1972–1980 (2020).
33. Bae, I.-G. & Park, B. All-self-metered solution-coating process in ambient air for the fabrication of efficient, large-area, and semi-transparent perovskite solar cells. *Sustain. Energy Fuels* **4**, 3115–3128 (2020).
34. Li, M. *et al.* Improving the conductivity of sol–gel derived NiO x with a mixed oxide composite to realize over 80% fill factor in inverted planar perovskite solar cells. *J. Mater. Chem. A* **7**, 9578–9586 (2019).
35. Bi, C. *et al.* Non-wetting surface-driven high-aspect-ratio crystalline grain growth for efficient hybrid perovskite solar cells. *Nat. Commun.* **6**, 1–7 (2015).
36. Zhang, H. *et al.* Pinhole-free and surface-nanostructured NiO x film by room-temperature solution process for high-performance flexible perovskite solar cells with good stability and reproducibility. *ACS Nano* **10**, 1503–1511 (2016).
37. Wang, W. *et al.* Highly sensitive low-bandgap perovskite photodetectors with response from ultraviolet to the near-infrared region. *Adv. Funct. Mater.* **27**, 1703953 (2017).
38. Chen, W. *et al.* Cesium doped NiOx as an efficient hole extraction layer for inverted planar perovskite solar cells. *Adv. Energy Mater.* **7**, 1700722 (2017).
39. Yang, X.-Y. & Chauhan, N. *Photoenergy and Thin Film Materials* (Wiley Online Library, New York, 2019).
40. Jiang, F., Choy, W. C., Li, X., Zhang, D. & Cheng, J. Post-treatment-free solution-processed non-stoichiometric NiOx nanoparticles for efficient hole-transport layers of organic optoelectronic devices. *Adv. Mater.* **27**, 2930–2937 (2015).
41. Ma, F. *et al.* Nickel oxide for inverted structure perovskite solar cells. *Journal of Energy Chemistry* (2020).
42. Yang, Z. *et al.* Stable low-bandgap Pb–Sn binary perovskites for tandem solar cells. *Adv. Mater.* **28**, 8990–8997 (2016).
43. Lee, K. *et al.* Enhanced efficiency and air-stability of NiO X-based perovskite solar cells via PCBM electron transport layer modification with Triton X-100. *Nanoscale* **9**, 16249–16255 (2017).
44. Chen, L.-C., Tien, C.-H., Tseng, Z.-L. & Ruan, J.-H. Enhanced efficiency of MAPbI3 perovskite solar cells with FAPbX3 perovskite quantum dots. *Nanomaterials* **9**, 121 (2019).
45. Zhang, H. *et al.* Improving the stability and performance of perovskite solar cells via off-the-shelf post-device ligand treatment. *Energy Environ. Sci.* **11**, 2253–2262 (2018).
46. Cheng, J. *et al.* Highly efficient planar perovskite solar cells achieved by simultaneous defect engineering and formation kinetic control. *J. Mater. Chem. A* **6**, 23865–23874 (2018).
47. Zhang, H. *et al.* Toward all room-temperature, solution-processed, high-performance planar perovskite solar cells: a new scheme of pyridine-promoted perovskite formation. *Adv. Mater.* **29**, 1604695 (2017).
48. Lu, H. *et al.* A self-powered and stable all-perovskite photodetector–solar cell nanosystem. *Adv. Funct. Mater.* **26**, 1296–1302 (2016).
49. Maculan, G. *et al.* CH3NH3PbCl3 single crystals: inverse temperature crystallization and visible-blind UV-photodetector. *J. Phys. Chem. Lett.* **6**, 3781–3786 (2015).
50. Dong, Y. *et al.* Improving all-inorganic perovskite photodetectors by preferred orientation and plasmonic effect. *Small* **12**, 5622–5632 (2016).
51. Zhao, Y. *et al.* Thick TiO2-based top electron transport layer on perovskite for highly efficient and stable solar cells. *ACS Energy Lett.* **3**, 2891–2898 (2018).
52. Wetzelaer, G., Kuik, M., Lenes, M. & Blom, P. Origin of the dark-current ideality factor in polymer: fullerene bulk heterojunction solar cells. *Appl. Phys. Lett.* **99**, 153506 (2011).
53. Tang, J. *et al.* High-performance inverted planar perovskite solar cells based on efficient hole-transporting layers from well-crystalline NiO nanocrystals. *Sol. Energy* **161**, 100–108 (2018).
54. Duan, L. *et al.* Relationship between the diode ideality factor and the carrier recombination resistance in organic solar cells. *IEEE J. Photovoltaics* **8**, 1701–1709 (2018).
55. Van den Meerakker, J., Kelly, J. & Notten, P. The minority carrier recombination resistance: a useful concept in semiconductor electrochemistry. *J. Electrochem. Soc.* **132**, 638 (1985).
56. Gao, Z. W. *et al.* Triple interface passivation strategy-enabled efficient and stable inverted perovskite solar cells. *Small Methods*, **4**, 2000478 (2020).
57. Wang, T. *et al.* Efficient inverted planar perovskite solar cells using ultraviolet/ozone-treated NiOx as the hole transport layer. *Solar RRL* **3**, 1900045 (2019).
58. He, Z. *et al.* Single-junction polymer solar cells with high efficiency and photovoltage. *Nat. Photonics* **9**, 174 (2015).
59. Zhang, H., Wang, H., Chen, W. & Jen, A. K. Y. CuGaO2: A promising inorganic hole-transporting material for highly efficient and stable perovskite solar cells. *Adv. Mater.* **29**, 1604984 (2017).
60. Ryu, S. *et al.* Light intensity-dependent variation in defect contributions to charge transport and recombination in a planar MAPbI 3 perovskite solar cell. *Sci. Rep.* **9**, 1–12 (2019).
61. Wu, G. *et al.* Perovskite/organic bulk-heterojunction integrated ultrasensitive broadband photodetectors with high near-infrared external quantum efficiency over 70%. *Small* **14**, 1802349 (2018).
62. Sim, K. M., Swarnkar, A., Nag, A. & Chung, D. S. Phase stabilized α-CsPbI3 perovskite nanocrystals for photodiode applications. *Laser Photonics Rev.* **12**, 1700209 (2018).
63. Xu, R. *et al.* Perovskite transparent conducting oxide for the design of a transparent, flexible, and self-powered perovskite photodetector. *ACS Appl. Mater. Interfaces.* **12**, 16462–16468 (2020).
64. Leung, S. F. *et al.* A self-powered and flexible organometallic halide perovskite photodetector with very high detectivity. *Adv. Mater.* **30**, 1704611 (2018).
65. Li, X. *et al.* Healing all-inorganic perovskite films via recyclable dissolution–recyrstallization for compact and smooth carrier channels of optoelectronic devices with high stability. *Adv. Func. Mater.* **26**, 5903–5912 (2016).

66. Liu, C. *et al.* Ultrasensitive solution-processed broad-band photodetectors using CH 3 NH 3 PbI 3 perovskite hybrids and PbS quantum dots as light harvesters. *Nanoscale* **7**, 16460–16469 (2015).
67. Bao, C. *et al.* Low-noise and large-linear-dynamic-range photodetectors based on hybrid-perovskite thin-single-crystals. *Adv. Mater.* **29**, 1703209 (2017).
68. Tong, S. *et al.* High-performance broadband perovskite photodetectors based on CH3NH3PbI3/C8BTBT heterojunction. *Adv. Electron. Mater.* **3**, 1700058 (2017).
69. Zhou, H. *et al.* Self-powered CsPbBr 3 nanowire photodetector with a vertical structure. *Nano Energy* **53**, 880–886 (2018).
70. Li, Y. *et al.* Ultrabroadband, ultraviolet to terahertz, and high sensitivity CH3NH3PbI3 perovskite photodetectors. *Nano Lett.* **20**, 5646–5654 (2020).
71. Zhang, X. *et al.* High-switching-ratio photodetectors based on perovskite CH3NH3PbI3 nanowires. *Nanomaterials* **8**, 318 (2018).
72. Zheng, E., Yuh, B., Tosado, G. A. & Yu, Q. Solution-processed visible-blind UV-A photodetectors based on CH 3 NH 3 PbCl 3 perovskite thin films. *J. Mater. Chem. C* **5**, 3796–3806 (2017).
73. Lee, Y. *et al.* High-performance perovskite–graphene hybrid photodetector. *Adv. Mater.* **27**, 41–46 (2015).
74. Gao, T., Zhang, Q., Chen, J., Xiong, X. & Zhai, T. Performance-enhancing broadband and flexible photodetectors based on perovskite/ZnO-nanowire hybrid structures. *Adv. Opt. Mater.* **5**, 1700206 (2017).
75. Waleed, A. *et al.* Lead-free perovskite nanowire array photodetectors with drastically improved stability in nanoengineering templates. *Nano Lett.* **17**, 523–530 (2017).
76. Zhou, J. *et al.* Lead-free perovskite derivative Cs2SnCl6− xBrx single crystals for narrowband photodetectors. *Adv. Opt. Mater.* **7**, 1900139 (2019).
77. Dou, L. *et al.* Solution-processed hybrid perovskite photodetectors with high detectivity. *Nat. Commun.* **5**, 1–6 (2014).

Acknowledgements

This research was supported by the Basic Science Research Program through the National Research Foundation of Korea (NRF), funded by the Korean Government (MEST) (2017R1A2A1A17069729 and 2020R1A2B5B03097060).

Author contributions

A. M. A., E. H. C., and B. P. conceived the work, designed the research strategy, and wrote the paper; B. P. obtained funding, supervised all the research, and E. H. C. and B. P. revised the manuscript. A. M. A., I.-G. B., Y. A., J. P., and H.-R. J. performed the experiments; all authors contributed to the analysis and interpretation of the data.

Competing interests

The authors declare no competing interests.

Additional information

Supplementary Information The online version contains supplementary material available at https://doi.org/10.1038/s41598-020-80640-3.

Correspondence and requests for materials should be addressed to B.P.

Reprints and permissions information is available at www.nature.com/reprints.

Publisher's note Springer Nature remains neutral with regard to jurisdictional claims in published maps and institutional affiliations.